Laser-induced resonances and photodissociation of H_2^+ in an adiabatic electronic-field representation

T. T. Nguyen-Dang and S. Manoli
Département de Chimie, Faculté des Sciences et de Genie, Université Laval, Québec, Canada G1K 7P4
(Received 18 March 1991)

Field-induced resonances in H_2^+ dressed by an intense laser field are calculated in the electric-field gauge (length gauge) in a fully coupled adiabatic electronic-field representation. Distinctions between diabatic and adiabatic resonance states are made. Adiabatic resonances are characterized in terms of shape and Feshbach resonances.

PACS number(s): 33.80.Gj, 42.50.Hz, 33.80.Wz

I. INTRODUCTION

The dynamics of molecules in intense fields ($I \geq 10^{10}$ W/cm^2) must be described using nonperturbative methods [1–5]. The dressed-molecule coupled-equation method is such a nonperturbative approach that has been used to describe molecular photodissociation [6–8] as well as other multiphoton processes [9–11]. This approach consists of considering the molecule and quantized radiation field together as a single conservative dressed system [3,4]. An often-invoked electronic-field basis for dressed systems is constructed from the direct product of field-free electronic states and photon-number states, defining the so-called *diabatic* electronic-field representation [5–8]. The coupled equations derived using this representation are of the same form as those obtained from the application of the Floquet theorem to the time evolution of a molecular system driven by a classical, periodic laser field [8,12,13]. Since radiative interactions are not included in the diabatic basis states and these interactions become stronger with increasing field intensity, a large number of coupled diabatic channels may be needed to obtain converged results even for a simple two-electronic-state problem such as the photodissociation of H_2^+ [8,13].

The diabatic basis can be subjected to a unitary transformation, dependent on nuclear coordinates, selected such that the dressed electronic Hamiltonian, which includes radiative couplings, is diagonalized. This results in the so-called *adiabatic* electronic-field basis, which constitutes an alternate representation for the dressed molecular system. In contrast with the diabatic coupled-equation scheme, the adiabatic channels become more decoupled with increasing field strength, suggesting that a reduced number of channels may be sufficient to obtain the same degree of convergence in the results. No full adiabatic coupled-equation calculations of photodissociation rates have been reported previously, even for H_2^+, because the field-induced nonadiabatic couplings were a major computational difficulty [14–16]. An attempt to exploit the decoupling that is characteristic of any adiabatic representation has recently been made in a so-called *semiadiabatic* treatment of H_2^+ [17]. In this approach, two semiadiabatic potentials, each obtained from a partial diagonalization of the full diabatic Hamiltonian matrix, are used in an effective diabatic coupled-equation scheme that was integrated using standard techniques. Residual nonadiabatic couplings resulting from the partial diagonalizations have simply been neglected. In a more qualitative vein, the adiabatic electronic-field representation has only been invoked to rationalize results obtained in diabatic calculations [8,13,17,18]. Finally, recent experimental observations of the dissociation of H_2^+ prepared in an intense laser field have also been analyzed in terms of dressed molecular potential-energy surfaces associated with the adiabatic representation [19,20] and have motivated new extensive diabatic calculations of the above-threshold ionization and dissociation of H_2 [21].

In the present work, full adiabatic coupled-equation calculations of laser-induced resonances in the photodissociation of H_2^+ are performed using a generalized Numerov integration algorithm recently developed to explicitly take into account nonadiabatic couplings [15,16]. For this ionic system, the transition dipole moment persists even at infinite separation, and hence scattering theory cannot be used to describe the photodissociation as a half-collision process in the diabatic representation. Thus, diabatic resonances reported by Chu [13] and He, Atabek, and Giusti-Suzor [8] were located as the complex eigenvalues of the complex dilatated Floquet Hamiltonian. In contrast, in the adiabatic representation, the nonadiabatic interactions vanish asymptotically and photodissociation can be viewed as a half-collision process. Hence adiabatic resonances reported in this work are obtained from the scattering matrix resulting from adiabatic coupled-equation integrations. The existence of fundamental differences between diabatic and adiabatic resonances is demonstrated. Adiabatic resonances are analyzed in terms of shape and Feshbach resonances. At high field intensities, overlap between these two types of resonances is found to be responsible for the formation of long-lived laser-induced adiabatic bound states.

II. DRESSED-MOLECULE MODEL FOR THE PHOTODISSOCIATION OF H_2^+

A. Diabatic and adiabatic electronic-field representations

The total Hamiltonian for a molecular system interacting with a quantized radiation field is

$$\hat{\mathcal{H}}(R)=\hat{T}_N+\hat{H}_{\rm el}(R)+\hat{H}_f+V_{\rm int}(R)\ , \tag{1}$$

where $\hat{T}_N$ is the nuclear kinetic-energy operator and $\hat{H}_f$ is the Hamiltonian for the quantized radiation field. The electronic Hamiltonian and the matter-field interaction potential, $\hat{H}_{\rm el}(R)$ and $V_{\rm int}(R)$, respectively, depend parametrically on the internuclear distance R. In this work, the photodissociation of H_2^+ is studied as transitions from bound states belonging to the $X\,^2\Sigma_g^+$ ground electronic manifold to dissociative ones of the $A\,^2\Sigma_u^+$ manifolds induced by a single-mode, monochromatic, linearly polarized radiation field. Accordingly,

$$\hat{H}_{\rm el}(R)=E_g(R)|1\sigma_g\rangle\langle 1\sigma_g|+E_u(R)|1\sigma_u\rangle\langle 1\sigma_u|\ , \tag{2}$$

where the states $|1\sigma_g\rangle$ and $|1\sigma_u\rangle$ vary parametrically with internuclear distance R,

$$\hat{H}_f=\hbar\omega(\hat{a}^\dagger\hat{a}+\tfrac{1}{2})\ , \tag{3}$$

$$\hat{V}_{\rm int}(R)=[V_{gu}(R)|1\sigma_g\rangle\langle 1\sigma_u|+{\rm H.c.}](\hat{a}+\hat{a}^\dagger)\ , \tag{4}$$

with

$$V_{gu}(R)=\left[\frac{\hbar\omega}{2\epsilon_0 V}\right]^{1/2}\langle 1\sigma_u|\boldsymbol{\mu}_{\rm el}(R)|1\sigma_g\rangle\cdot\boldsymbol{\epsilon} \tag{5}$$

expressed in SI units where ϵ_0 is the permittivity constant of a vacuum. The $\hat{a}^\dagger$ and $\hat{a}$ are creation and annihilation operators for the single-mode radiation field of frequency ω and polarization $\boldsymbol{\epsilon}$ in the quantized cavity of volume V, and $\boldsymbol{\mu}_{\rm el}(R)$ is the parametrically R-dependent transition dipole moment operator. The solutions of the time-independent Schrödinger equation

$$\hat{\mathcal{H}}(R)|\Psi\rangle=E|\Psi\rangle \tag{6}$$

determine the stationary states of the dressed molecular system. These are written as

$$|\Psi\rangle=\int d\mathbf{R}\sum_n[\chi_g^n(\mathbf{R})|1\sigma_g\rangle+\chi_u^n(\mathbf{R})|1\sigma_u\rangle]|n\rangle|\mathbf{R}\rangle\ , \tag{7}$$

$$|\Psi\rangle\equiv\sum_n[|\chi_g^n(\mathbf{R})\rangle|1\sigma_g\rangle+|\chi_u^n(\mathbf{R})\rangle|1\sigma_u\rangle]|n\rangle\ , \tag{8}$$

where $|n\rangle$ are eigenstates of $\hat{H}_f$ with corresponding eigenvalue $(n+\frac{1}{2})\hbar\omega$. Using (7) or (8) in (6) gives the infinite set of coupled equations for the nuclear amplitudes $\chi_u^{n-1}(\mathbf{R})$ and $\chi_g^n(\mathbf{R})$:

$$[\hat{T}_N+E_g(R)+n\hbar\omega-E]|\chi_g^n(\mathbf{R})\rangle = V_{gu}(R)[\sqrt{n+1}\,|\chi_u^{n+1}(\mathbf{R})\rangle+\sqrt{n}\,|\chi_u^{n-1}(\mathbf{R})\rangle]\ , \tag{9}$$

$$[\hat{T}_N+E_u(R)+(n-1)\hbar\omega-E]|\chi_u^{n-1}(\mathbf{R})\rangle = V_{gu}(R)[\sqrt{n}\,|\chi_g^n(\mathbf{R})\rangle+\sqrt{n-1}\,|\chi_g^{n-2}(\mathbf{R})\rangle]\ . \tag{10}$$

For the laser intensities under consideration in this work, the square roots of the photon numbers in (9) and (10) are all approximately equal to $\sqrt{n}$ so that the radiative coupling potential may be expressed using

$$\tilde{V}_{gu}(R)=\left[\frac{n\hbar\omega}{2\epsilon_0 V}\right]^{1/2}\langle 1\sigma_u|\boldsymbol{\mu}_{\rm el}(R)|1\sigma_g\rangle\cdot\boldsymbol{\epsilon}\ . \tag{11}$$

Using the expression for the field intensity

$$I=cn\hbar\omega/V\ , \tag{12}$$

$\tilde{V}_{gu}(R)$ can be written in terms of intensity

$$\tilde{V}_{gu}({\rm cm}^{-1})=5.85\times10^{-4}[I({\rm W/cm^2})]^{1/2}\times[\langle 1\sigma_u|\boldsymbol{\mu}_{\rm el}(R)|1\sigma_g\rangle\cdot\boldsymbol{\epsilon}]({\rm a.u.})\ . \tag{13}$$

The coupled equations (9) and (10) can be expressed in matrix form:

$$[\hat{T}_N+E\underline{I}+\underline{V}^{\rm diab}(R)]\underline{X}^{\rm diab}(\mathbf{R})=0\ , \tag{14}$$

where $\underline{I}$ is the identity matrix, $\underline{V}^{\rm diab}(R)$ is the diabatic potential matrix

$$\underline{V}^{\rm diab}(R)=\begin{pmatrix} \cdots & & & & & \\ \vdots & \ddots & & 0 & 0 & 0 \\ & \underline{V}_{gu}^T(R) & \underline{F}^{(1)}(R) & \underline{V}_{gu}(R) & 0 & 0 \\ & 0 & \underline{V}_{gu}^T(R) & \underline{F}^{(0)}(R) & \underline{V}_{gu}(R) & 0 \\ & 0 & 0 & \underline{V}_{gu}^T(R) & \underline{F}^{(-1)}(R) & \underline{V}_{gu}(R) \\ & 0 & 0 & 0 & \ddots & \vdots \\ & & & & \cdots & \end{pmatrix} \tag{15}$$

with

$$\underline{V}_{gu}(R)=\begin{bmatrix}0 & 0\\ \tilde{V}_{gu}(R) & 0\end{bmatrix}. \tag{16}$$

$\underline{F}^{(p)}$ is the two-dimensional matrix

$$\underline{F}^{(p)}(R)=\begin{bmatrix}E_g(R)+2p\hbar\omega & \tilde{V}_{gu}(R)\\ \tilde{V}_{gu}(R) & E_u(R)+(2p-1)\hbar\omega\end{bmatrix}, \tag{17}$$

and the $\underline{X}^{\text{diab}}(\mathbf{R})$ is a vector consisting of the diabatic nuclear states

$$\underline{X}^{\text{diab}}(\mathbf{R})=\begin{bmatrix}\vdots\\ |\chi_g^{n+2}(\mathbf{R})\rangle\\ |\chi_u^{n+1}(\mathbf{R})\rangle\\ |\chi_g^{n}(\mathbf{R})\rangle\\ |\chi_u^{n-1}(\mathbf{R})\rangle\\ |\chi_u^{n-1}(\mathbf{R})\rangle\\ |\chi_g^{n-2}(\mathbf{R})\rangle\\ |\chi_u^{n-3}(\mathbf{R})\rangle\\ \vdots\end{bmatrix}. \tag{18}$$

In principle, these matrices must be of infinite dimension. The zeroth-order $|1\sigma_g\rangle|n\rangle$ and $|1\sigma_u\rangle|n-1\rangle$ states in (9) and (10) are coupled by *potential* radiative couplings and hence, they constitute a diabatic basis. The matrix equations (14)–(18) have also been derived semiclassically from considerations of the time-dependent Schrödinger equation in a periodic field and the two-dimensional matrix in (17) is exactly equivalent to a single Floquet block in that formalism [8,12,13]. As depicted by (15), the diabatic potential matrix consists of coupled Floquet blocks. For weak fields, i.e., low intensities ($I \le 10^{10}$ W/cm^2), the couplings between Floquet blocks can be neglected, defining the rotating wave approximation (RWA), and a single Floquet block will suffice to give converged results. At higher intensities, an increased number of blocks is required to ensure convergence. This relationship between intensity and the number of Floquet blocks is characteristic of calculations in the diabatic electronic-field basis.

Alternatively, an electronic-field basis can be defined in which the potential matrix is diagonal. This can be achieved by subjecting $\underline{X}^{\text{diab}}(\mathbf{R})$ to an orthogonal transformation

$$\underline{X}^{\text{ad}}(\mathbf{R})=\underline{C}(R)\underline{X}^{\text{diab}}(\mathbf{R}) \tag{19}$$

such that

$$\underline{V}^{\text{ad}}(R)=\underline{C}(R)^{\dagger}\underline{V}^{\text{diab}}(R)\underline{C}(R) \tag{20}$$

is diagonal. Figure 1 illustrates the adiabatic channel potentials obtained from the diagonalization of a four-Floquet-block diabatic potential matrix. In this figure, and henceforth in this work, centrifugal terms obtained from the angular expansion of the nuclear amplitudes are implicitly included in the diabatic potentials. The resulting rotational state couplings are neglected and the radial adiabatic matrix equation to be solved is

$$-\frac{\hbar^2}{M_H}\left[\frac{d^2}{dR^2}+\underline{Q}(R)\frac{d}{dR}+\underline{W}^{\text{ad}}(R)\right]\underline{X}^{\text{ad}}(R)=0\,, \tag{21}$$

where

$$\underline{Q}(R)=2\underline{C}(R)^{\dagger}\left[\frac{d}{dR}\underline{C}(R)\right] \tag{22}$$

is the nonadiabatic coupling matrix and

$$\underline{W}^{\text{ad}}(R)=\frac{M_H}{\hbar^2}[E\underline{I}-\underline{V}^{\text{ad}}(R)]+\underline{C}(R)^{\dagger}\frac{d^2}{dR^2}\underline{C}(R)\,. \tag{23}$$

As the intensity increases, the nonadiabatic couplings in the skew-symmetric matrix $\underline{Q}(R)$ and in the last term of (23) decrease in magnitude and become less localized. Thus, for a given sufficiently strong field intensity, the dimension of the matrix equation to be solved in the adiabatic representation will be smaller than the dimension of the corresponding diabatic matrix equation.

In the past, this adiabatic electronic-field representation has only been evoked in some discussions of molecular dynamics to qualitatively rationalize high-intensity results obtained by integration of diabatic coupled equations [8,13,17,18]. The adiabatic-coupled-equation integrations were not done, or even attempted, because of

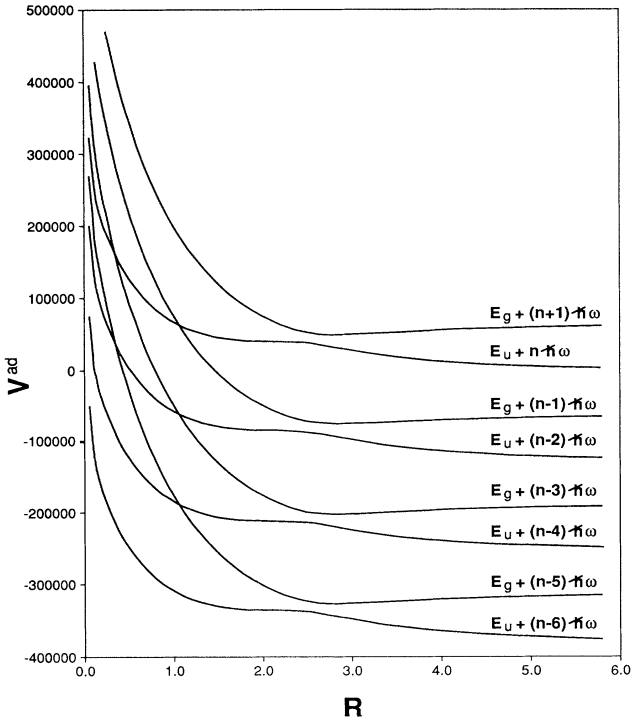

FIG. 1. Adiabatic potentials (in cm^{-1}) vs R (in a.u.) obtained from the diagonalization of an eight-channel diabatic potential matrix constructed from the dressing of the $X\,^2\Sigma_g$ and $A\,^2\Sigma_u$ states of H_2^+ by a field of wavelength λ equal to 1600 Å and at an intensity of 8.80×10^{13} W/cm^2. The labels refer to the dressed diabatic potentials.

the lack of a straightforward algorithm for solving differential equations coupled by kinetic terms such as those represented in the matrix equation (21). The generalization of the Numerov integration formula reported recently by Nguyen-Dang, Durocher, and Atabek [15], henceforth called the NDDA algorithm, has been developed for this purpose. With this method, the adiabatic coupled equations (21) for the photodissociation of H_2^+ have been integrated and the solutions have been studied with emphasis placed on the analysis and identification of laser-induced resonances. In the diabatic and adiabatic representations, resonances arise from the mixing of bound dressed states with those of the dissociative continua and are reflected by the strong asymptotic energy dependence of the amplitudes associated with the so-called *open* channels. In either representation, a given channel is said to be open at an energy E if the channel potential $E_k(R)$ obeys

$$\lim_{R\to\infty}[E-E_k(R)]>0 . \tag{24}$$

Conversely, channels that do not obey (24) are said to be *closed*. In the dressed diabatic representation, all laser-induced resonances are Feshbach resonances but in the adiabatic representation not all resonances are Feshbach type. Furthermore, adiabatic Feshbach resonances are not generally the unitary equivalents of diabatic ones.

B. Diabatic and adiabatic Feshbach resonances

In Feshbach resonance theory, the partitioning of the total state of the system $|\Psi\rangle$ into open- and closed-channel components using orthogonal operators $\hat{P}$ and $\hat{Q}$, respectively [22,23],

$$|\Psi\rangle=\hat{P}|\Psi\rangle+\hat{Q}|\Psi\rangle , \tag{25}$$

results in the coupled equations

$$[E-\hat{P}\hat{\mathcal{H}}(R)\hat{P}]\hat{P}|\Psi\rangle-\hat{P}\hat{\mathcal{H}}(R)\hat{Q}\hat{Q}|\Psi\rangle=0 , \tag{26}$$

$$[E-\hat{Q}\hat{\mathcal{H}}(R)\hat{Q}]\hat{Q}|\Psi\rangle-\hat{Q}\hat{\mathcal{H}}(R)\hat{P}\hat{P}|\Psi\rangle=0 . \tag{27}$$

The formal solution of (26) gives the open-channel wave function

$$\hat{P}|\Psi\rangle=|\Psi^0\rangle+G_{PP}^{0+}[\hat{\mathcal{H}}]\hat{H}_{PQ}\hat{Q}|\Psi\rangle , \tag{28}$$

where henceforth

$$\hat{H}_{PP}=\hat{P}\hat{\mathcal{H}}(R)\hat{P},\quad \hat{H}_{PQ}=\hat{P}\hat{\mathcal{H}}(R)\hat{Q} ,$$
$$\hat{H}_{QQ}=\hat{Q}\hat{\mathcal{H}}(R)\hat{Q},\quad \hat{H}_{QP}=\hat{Q}\hat{\mathcal{H}}(R)\hat{P} , \tag{29}$$

$|\Psi^0\rangle$ is the solution of the uncoupled open channel equation

$$(E-\hat{H}_{PP})|\Psi^0\rangle=0 , \tag{30}$$

and the Green's operator [24]

$$G_{PP}^{0+}[\hat{\mathcal{H}}]\equiv\lim_{\epsilon\to 0+}(E+i\epsilon-\hat{H}_{PP})^{-1} \tag{31}$$

is an energy-dependent functional of the Hamiltonian $\hat{\mathcal{H}}(R)$. The corresponding closed-channel equation defines the level operator

$$\hat{L}_{QQ}[\hat{H}]\equiv\hat{H}_{QQ}+\hat{H}_{QP}G_{PP}^{0+}[\hat{\mathcal{H}}]\hat{H}_{PQ} , \tag{32}$$

which has eigenstates and eigenvalues

$$\hat{L}_{QQ}[\hat{\mathcal{H}}]|X_j\rangle=\epsilon_j(E)|X_j\rangle , \tag{33}$$

$$\epsilon_j(E)=\Omega_j(E)-\tfrac{1}{2}i\Gamma_j(E) \tag{34}$$

that are parametrically energy dependent. Eigenstates of $\hat{L}_{QQ}[\hat{\mathcal{H}}]$ are defined as *Feshbach resonance states* and the real and imaginary parts of each eigenvalue define the position and width of the corresponding resonance, respectively [22]. The open-channel wave function can be expressed in terms of a linear combination of these resonance states as

$$\hat{P}|\Psi\rangle=|\Psi^0\rangle+\sum_j\frac{\langle X_j^*|\hat{H}_{QP}|\Psi^0\rangle}{E-\epsilon_j}G_{PP}^{0+}[\hat{\mathcal{H}}]\hat{H}_{PQ}|X_j\rangle . \tag{35}$$

In general, the uncoupled open-channel wave function $|\Psi^0\rangle$ is assumed to be mildly energy dependent. Furthermore, if the coupling between the open- and closed-channel wave functions is small, the resonance states and their corresponding eigenvalues are also mildly energy dependent. Hence the major energy variation of the open-channel wave function about the position of a given resonance is due to the denominator of the corresponding term in the summation of (35); as the energy E approaches the position of the kth resonance, the $|X_k\rangle$ resonance state becomes the major component of the open-channel wave function. In this isolated resonance approximation the open-channel wave function can be written [22,23]

$$\hat{P}|\Psi\rangle=|\tilde{\Psi}^0\rangle+\frac{\langle X_k^*|\hat{H}_{QP}|\Psi^0\rangle}{E-\epsilon_k}G_{PP}^{0+}[\hat{\mathcal{H}}]\hat{H}_{PQ}|X_k\rangle \tag{36}$$

in a given neighborhood of the kth isolated resonance. The energetically slowly varying $j\neq k$ terms of the summation of (35) have been included in $|\tilde{\Psi}^0\rangle$. According to (36), in a given energy range, the abrupt variation of $\hat{P}|\Psi\rangle$ signals the presence of a Feshbach resonance. This assumes $|\tilde{\Psi}^0\rangle$ does not intrinsically exhibit such a resonant behavior in that same energy range, which is the case in the diabatic basis because the uncoupled open-channel potentials are purely repulsive and cannot support resonance states; resonance states are created strictly as a consequence of coupling between the open- and closed-channel wave functions. Hence diabatic resonances are purely Feshbach resonances. On the other hand, in the adiabatic basis, the adiabatic uncoupled open-channel wave function, the adiabatic counterpart of $|\tilde{\Psi}^0\rangle$ in (36), is a mixture of diabatic open- and closed-channel amplitudes induced by the radiative coupling. Consequently, the adiabatic uncoupled open-channel potential *may support resonances* of the type *shape*. As the intensity increases, overlap between Feshbach and shape resonances will occur in addition to overlap between pure Feshbach resonances [this requires that, in the sum of (35), more than a single term be taken into account]. Only overlap between pure Feshbach resonances can

occur in the diabatic basis. The onset of Feshbach resonance overlap is also expected to occur differently in the two bases because the adiabatic and diabatic non-Hermitian level operators are not unitary equivalents, unlike Hermitian operators representing a given physical observable in the two representations.

As an illustration, consider the two-channel problem defined by the H_2^+ dressed-molecule Hamiltonian (1) truncated to a single Floquet block so that the diabatic electronic-field basis is restricted to the $|1\sigma_g\rangle|n\rangle$ and $|1\sigma_u\rangle|n-1\rangle$ states, henceforth abbreviated as $|g,n\rangle$ and $|u,n-1\rangle$, respectively. The open- and closed-channel projection operators are then

$$\hat{P}=|u,n-1\rangle\langle u,n-1|, \quad \hat{Q}=|g,n\rangle\langle g,n| , \tag{37}$$

and (26) and (27) yield the diabatic coupled equations (9) and (10) identically provided the nuclear states are defined by

$$|\chi_{1(2)}^{d}(\mathbf{R})\rangle=\langle g,n(u,n-1)|\Psi\rangle \tag{38}$$

and the open- and closed-channel wave functions are identified as

$$\hat{P}|\Psi\rangle=|\chi_2^d(\mathbf{R})\rangle|u,n-1\rangle, \quad \hat{Q}|\Psi\rangle=|\chi_1^d(\mathbf{R})\rangle|g,n\rangle , \tag{39}$$

respectively. Therefore the open-channel solutions of the diabatic coupled equations (9) and (10) are related to the eigenstates of the diabatic level operator $\hat{L}_{QQ}[\hat{\mathcal{H}}]$ according to (35). Hence the asymptotic behavior of these solutions can be used to determine the eigenvalues of $\hat{L}_{QQ}[\hat{\mathcal{H}}]$ that correspond to the position and width of the diabatic resonances.

In the adiabatic representation, the unitary transformation $\hat{\mathcal{R}}$,

$$\hat{\mathcal{R}}=\cos\vartheta(R)(\hat{Q}+\hat{P}) +\sin\vartheta(R)(|u,n-1\rangle\langle g,n|-|g,n\rangle\langle u,n-1|) , \tag{40}$$

where $\vartheta(R)$ is an angle of rotation, is implicitly associated with the rotation matrix $\underline{C}(R)$ of (19) and defines new electronic-field basis vectors

$$|1\rangle=\hat{\mathcal{R}}|g,n\rangle=\cos\vartheta(R)|g,n\rangle+\sin\vartheta(R)|u,n-1\rangle \tag{41}$$

$$|2\rangle=\hat{\mathcal{R}}|u,n-1\rangle=-\sin\vartheta(R)|g,n\rangle+\cos\vartheta(R)|u,n-1\rangle . \tag{42}$$

In this new basis, defining the open- and closed-channel projection operators as

$$\hat{P}'=\hat{\mathcal{R}}\hat{P}\hat{\mathcal{R}}^{\dagger}=|2\rangle\langle 2|, \quad \hat{Q}'=\hat{\mathcal{R}}\hat{Q}\hat{\mathcal{R}}^{\dagger}=|1\rangle\langle 1| , \tag{43}$$

respectively, and selecting $\vartheta(R)$ such that the transformed dressed electronic-field Hamiltonian is diagonal,

$$\hat{H}_{\rm el}(R)+\hat{H}_f+V_{\rm int}(R)=W_{-}^{\rm ad}(R)\hat{P}'+W_{+}^{\rm ad}(R)\hat{Q}' , \tag{44}$$

where

$$W_{\pm}^{\rm ad}(R)=\tfrac{1}{2}[E_g(R)+E_u(R)] \pm\tfrac{1}{2}\{[E_g(R)-E_u(R)]^2+4V_{gu}^2(R)\}^{1/2} \tag{45}$$

are the adiabatic potentials, the coupled equations (26) and (27) become the adiabatic coupled equations

$$[E-\hat{T}_N-\tilde{W}_{-}^{\rm ad}(R)]|\chi_2^{\rm ad}(\mathbf{R})\rangle =\frac{\hbar^2}{2\mu}\left[2\left[\frac{d}{dR}\vartheta(R)\right]\frac{d}{dR}+\frac{d^2}{dR^2}\vartheta(R)\right]|\chi_1^{\rm ad}(\mathbf{R})\rangle , \tag{46}$$

$$[E-\hat{T}_N-\tilde{W}_{+}^{\rm ad}(R)]|\chi_1^{\rm ad}(\mathbf{R})\rangle =-\frac{\hbar^2}{2\mu}\left[2\left[\frac{d}{dR}\vartheta(R)\right]\frac{d}{dR}+\frac{d^2}{dR^2}\vartheta(R)\right]|\chi_2^{\rm ad}(\mathbf{R})\rangle , \tag{47}$$

where

$$\tilde{W}_{\pm}^{\rm ad}(R)=W_{\pm}^{\rm ad}(R)+\frac{\hbar^2}{2\mu}\left[\frac{d}{dR}\vartheta(R)\right]^2 , \tag{48}$$

and the adiabatic nuclear states are given by

$$|\chi_{1(2)}^{\rm ad}(\mathbf{R})\rangle=\langle g,n(u,n-1)|\hat{\mathcal{R}}^{\dagger}|\Psi\rangle=\langle 1(2)|\Psi\rangle . \tag{49}$$

Just as the solutions of the diabatic coupled equations can be expressed in terms of eigenstates of the level operator $\hat{L}_{QQ}[\hat{\mathcal{H}}]$ where $\hat{\mathcal{H}}(R)$ is the Hamiltonian (1) with (2)–(5), the solutions of the coupled equations (46) and (47) can be expressed in terms of eigenstates of the level operator $\hat{L}_{Q'Q'}[\hat{\mathcal{H}}]$. The resonant behavior exhibited by these solutions can be used to determine the position and width of adiabatic Feshbach resonances.

The adiabatic level operator $\hat{L}_{Q'Q'}[\hat{\mathcal{H}}]$ differs from $\hat{L}_{Q'Q'}[\hat{\mathcal{H}}^{\rm ad}]$, which is the unitary transform of the diabatic level operator $\hat{L}_{QQ}[\hat{\mathcal{H}}]$, $\hat{\mathcal{H}}^{\rm ad}$ being the image of $\hat{\mathcal{H}}$ under the unitary transformation represented by $\hat{\mathcal{R}}$. Hence there is no unitary relationship between the adiabatic and diabatic level operators. Therefore, adiabatic and diabatic Feshbach resonances are not unitary equivalents, although physical observables such as branching ratios must be invariant under the unitary transformation $\hat{\mathcal{R}}$.

III. COMPUTATIONAL ASPECTS

A. Potentials and couplings

The electronic states $X\,^2\Sigma_g^+$ and $A\,^2\Sigma_u^+$ involved in the photodissociation of H_2^+ are represented by the model potentials defined by Bunkin and Tugov [25]

$$E_1(R)=D_0\exp[-\alpha(R-R_{\rm eq})] \times\{\exp[-\alpha(R-R_{\rm eq})]-2t_i\}, \quad i=g,u \tag{50}$$

where the subscripts g and u refer to the bound and dissociative potentials, respectively. The values of the parameters are

$$t_g=1.0,\quad t_u=-1.11,\quad D_0-=2.7925\ \text{eV}\ ,$$
$$\alpha=0.72a_0^{-1},\quad R_{\text{eq}}=2.0a_0\ . \tag{51}$$

The transition dipole moment in (13) is given by

$$\langle 1\sigma_u|\mu_{\text{el}}(R)|1\sigma_g\rangle\cdot\epsilon = \mu(R_{\text{eq}})+\frac{\mu'(R_{\text{eq}})}{\alpha y}\{1-\exp[-\alpha y(R-R_{\text{eq}})]\}\ , \tag{52}$$

where

$$\mu(R_{\text{eq}})=1.07a_0e,\quad \mu'(R_{\text{eq}})=0.396e\ ,$$
$$y=-0.055\ . \tag{53}$$

The potentials (50) with parameters (51) and the dipole moment (52) and (53) have been used by Chu [13] and He, Atabek, and Giusti-Suzor [8] in their studies of the laser-induced diabatic resonances of H_2^+.

The diabatic potential matrix $\underline{V}^{\text{diab}}(R)$, constructed from (15)–(17) using the potentials defined by (50) and (51), is diagonalized to give the adiabatic potential matrix (20). The rotation matrix $\underline{C}(R)$ can be used to calculate the nonadiabatic couplings (22) and (23). However, instead of differentiating $\underline{C}(R)$ with respect to R numerically, the nonadiabatic couplings have been calculated semianalytically using Hellmann–Feynman-type expressions. The R derivative of (20),

$$\frac{d\underline{V}^{\text{ad}}}{dR}(R)=\tfrac{1}{2}[\underline{V}^{\text{ad}}(R)\underline{Q}(R)-\underline{Q}(R)\underline{V}^{\text{ad}}(R)] +\underline{C}^{\dagger}(R)\frac{d\underline{V}}{dR}^{\text{diab}}(R)\underline{C}(R)\ , \tag{54}$$

is used to derive the off-diagonal elements of the $\underline{Q}$ matrix

$$Q_{ij}=\frac{2\left[\underline{C}^{\dagger}(R)\dfrac{d\underline{V}^{\text{diab}}(R)}{dR}\underline{C}(R)\right]_{ij}}{V_{jj}^{\text{ad}}-V_{ii}^{\text{ad}}}\ . \tag{55}$$

Similarly, the second derivative of (20) gives the off-diagonal elements of $\underline{W}^{\text{ad}}(R)$ as

$$\left[\underline{C}(R)^{\dagger}\frac{d^2}{dR^2}\underline{C}(R)\right]_{ij}=\left[\tfrac{1}{4}\underline{Q}^2(R)+\frac{1}{2}\frac{d\underline{Q}(R)}{dR}\right]_{ij}\ . \tag{56}$$

The nonadiabatic couplings calculated in this way are more accurate and lead to better computational stability and efficiency in the use of the NDDA algorithm than those calculated from the numerical differentiation of $\underline{C}(R)$.

B. Integration method

Using the NDDA algorithm to solve the adiabatic coupled equations for the photodissociation of H_2^+, the matrix equation (21), along with (22) and (23), is transformed into the three-point recurrence formula

$$\begin{aligned}&\tfrac{1}{4}\{\underline{D}(R-h)^{-1}[\underline{I}-\tfrac{1}{6}h\underline{Q}(R-h)]+\underline{D}(R+h)^{-1}[3\underline{I}+\tfrac{7}{6}h\underline{Q}(R+h)+\tfrac{1}{3}h^2\underline{W}^{\text{ad}}(R+h)]\}\underline{X}^{\text{ad}}(R+h)\\ &-\tfrac{1}{3}\{\underline{D}(R-h)^{-1}[3\underline{I}-h\underline{Q}(R-h)-\tfrac{5}{4}h^2\underline{W}^{\text{ad}}(R)+\tfrac{1}{4}h^3\underline{Q}(R-h)\underline{W}^{\text{ad}}(R)]\ .\\ &+\underline{D}(R+h)^{-1}[3\underline{I}+h\underline{Q}(R+h)-\tfrac{5}{4}h^2\underline{W}^{\text{ad}}(R)-\tfrac{1}{4}h^3\underline{Q}(R+h)\underline{W}^{\text{ad}}(R)]\}\underline{X}^{\text{ad}}(R)\\ &+\tfrac{1}{4}\{\underline{D}(R+h)^{-1}[\underline{I}+\tfrac{1}{6}h\underline{Q}(R+h)]+\underline{D}(R-h)^{-1}[3\underline{I}-\tfrac{7}{6}h\underline{Q}(R-h)+\tfrac{1}{3}h^2\underline{W}^{\text{ad}}(R-h)]\}\underline{X}^{\text{ad}}(R-h)=0\ ,\end{aligned} \tag{57}$$

where h is the integration step and

$$\underline{D}(R\pm h)\equiv\underline{I}\mp\tfrac{5}{6}h\underline{Q}(R)\pm\tfrac{1}{3}h\underline{Q}(R\pm h) -\tfrac{1}{6}h^2\underline{Q}(R\pm h)\underline{Q}(R)\ . \tag{58}$$

The original three-point recurrence formula given in Ref. [15] has been reformulated in this work for computational efficiency to give (57) and (58). If the nonadiabatic coupling $\underline{Q}(R)$ is zero, the NDDA integration formula (57) reduces to the standard Numerov integration formula for diabatic coupled equations. The error in the recurrence relation is of sixth order with respect to the integration stepsize h [15]. As noted in Ref. [15], care must be exercised to properly cover regions where the nonadiabatic couplings exhibit strong variations. Typically, these regions are neighborhoods of avoided crossings whose ranges increase with increasing diabatic coupling strength, which, in the present context, corresponds to increasing field intensity. Hence, in the neighborhood of an avoided crossing, the stepsize h is reduced by a factor of 2^{ndiv} using the method described in Ref. [15]. The integration is more sensitive to this coverage than other parameters. The results presented in the next section have converged with respect to all integration parameters. Typical values for these parameters are given in Table I for one-Floquet-block (two-channel) and two-Floquet-block (four-channel) integrations with a laser wavelength of 1600 Å at an intermediate intensity of 1.3×10^{12} W/cm^2.

The coupled equations were integrated starting from a value of R close to zero, $R_{\text{beg}}=h$, outward to a value of R sufficiently large, R_{end}, to ensure that the interchannel

TABLE I. Sample integration parameters to be used in one- and two-Floquet-block calculations. $\lambda = 1600$ Å and $I \simeq 1.27 \times 10^{12}$ W/cm^2.

	One block	Two blocks
Number of channels	2	4
Number of open channels	1	3
Integration step $\equiv h$	2.5×10^{-3} a.u.	2.5×10^{-3} a.u.
Initial integration point $\equiv R_{\text{beg}}$	2.5×10^{-3} a.u.	2.5×10^{-3} a.u.
Final integration point $\equiv R_{\text{end}}$	5.8 a.u.	5.8 a.u.
Number of crossings	1	2
Crossing point $\equiv R_x$	2.5822 a.u.	2.5822 a.u.
Initial integration point of crossing region $\equiv R_{\text{cm}}$	1.4722 a.u.	1.4722 a.u.
Final integration point of crossing region $\equiv R_{\text{cp}}$	3.6472 a.u.	3.6472 a.u.
Value of ndiv (integration step in crossing region is $h/2^{\text{ndiv}}$)	1	1
Crossing point energy (above minimum of bound state)	2676.8 cm^{-1}	2676.8 cm^{-1}
Crossing point $\equiv R_x$		1.0563 a.u.
Initial integration point of crossing region $\equiv R_{\text{cm}}$		1.0538 a.u.
Final integration point of crossing region $\equiv R_{\text{cp}}$		1.0588 a.u.
Value of ndiv (integration step in crossing region is $h/2^{\text{ndiv}}$)		9
Crossing point energy (above minimum of bound state)		21524.8 cm^{-1}

couplings have attained values at least three orders of magnitude smaller than their maxima at the avoided crossings. Neglecting these small couplings in this asymptotic region, the nuclear wave functions are fitted to scattering boundary conditions. The resonance shifts and widths reported in this work were obtained using $R_{\text{end}} = 5.8$ a.u. They have been found to be stable with respect to variations in R_{end}, which, in certain test cases, i.e., wavelengths of 1000 and 1600 Å and an intensity of 1.41×10^{13} W/cm^2, was varied up to 14 a.u. However, calculations of branching ratios, which have not been attempted in this work, will require the residual asymptotic nonadiabatic couplings to be properly taken into account, as these ratios are much more sensitive to the value of R_{end} than resonance positions and widths. The asymptotic analysis of the nuclear wave functions gives an energy-dependent S matrix $\underline{S}(E)$ for the coupled adiabatic problem. The determinant of $\underline{S}(E)$ can be expressed in terms of a phase

$$\det[\underline{S}(E)] = \exp[2i\delta(E)] , \tag{59}$$

whose sharp variation with respect to energy E signals the presence of a resonance. Furthermore, the S matrix associated with the uncoupled open-channel wave functions, $\underline{S}_0$ is also calculated and phase analyzed in the same manner to identify pure shape resonances. A reduced S matrix for the coupled problem, defined as

$$\underline{S}_{\text{red}}(E) = \underline{S}_0^{-1/2} \underline{S}(E) \underline{S}_0^{-1/2} , \tag{60}$$

will also be used in conjunction with the unreduced S matrix $\underline{S}(E)$ to identify Feshbach resonances by the same type of phase analysis using

$$\det[\underline{S}_{\text{red}}(E)] = \exp\{2i[\delta(E) - \delta_0(E)]\} , \tag{61}$$

where $\delta_0(E)$ is the phase associated with the determinant of $\underline{S}_0(E)$. At intensities where no overlap between pure shape and Feshbach resonances occurs, $\underline{S}_{\text{red}}(E)$ and $\underline{S}(E)$ should possess a common set of resonances that are necessarily of the Feshbach type. According to (59) and (61), a given pure shape resonance, associated with an abrupt variation in $\delta_0(E)$ and hence detected through $\underline{S}_0(E)$, could only be observed in either $\underline{S}_{\text{red}}(E)$ or $\underline{S}(E)$ but not in both. Overlap of Feshbach and shape resonances is signaled by the deviation of $\underline{S}(E)$ resonances from those associated with $\underline{S}_{\text{red}}(E)$.

IV. RESULTS

A. Interblock coupling effects

Table II shows the effects of interblock coupling on the position and width of the first resonance obtained using the reduced S matrix $\underline{S}_{\text{red}}(E)$ of (60) for field intensities ranging from 10^{11} to 10^{14} W/cm^2 and for the wavelength λ equal to 1000, 1200, 1400, and 1600 Å. Henceforth the position of a resonance is given as the energy shift ΔE relative to the $v = 0$, $J = 1$ rovibrational energy level of the electronic ground state of H_2^+. These effects are revealed by comparing the results of integrations using one, two, and three Floquet blocks. For these wavelengths and at

TABLE II. Comparison of the shift ΔE and width Γ (in cm^{-1}) of the first adiabatic resonance calculated from the reduced S matrix $\underline{S}_{red}(E)$ using one, two, and three Floquet blocks for wavelengths 1000, 1200, 1400, and 1600 Å and for intensities up to 10^{14} W/cm^2. The shift ΔE represents the resonance position relative to the rovibrational ($v=0$, $J=1$) level of the electronic ground state of H_2^+. $x[y]$ represents $x \times 10^y$.

		Two channels		Four channels		Six channels	
λ	I (W/cm^2)	$\Gamma/2$	ΔE	$\Gamma/2$	ΔE	$\Gamma/2$	ΔE
1000 Å	1.41[11]	3.43	1.40	3.44	1.40	3.39	1.40
	4.08[11]	9.93	6.11	10.00	6.11	9.90	6.11
	8.80[11]	21.60	14.48	21.73	14.48	21.09	14.48
	1.27[12]	31.23	21.33	31.38	21.33	31.22	21.33
	2.85[12]	71.24	49.38	71.39	49.37	71.47	49.37
	5.08[12]	128.23	88.62	128.36	88.58	128.56	88.59
	6.88[12]	175.32	120.89	175.47	120.82	175.39	120.83
	9.00[12]	228.63	157.84	228.84	157.72	228.88	157.72
	1.41[13]	345.31	243.68	345.58	243.34	345.68	243.35
	2.03[13]	452.28	336.38	452.14	335.47	452.04	335.49
	3.17[13]	533.36	425.44	530.66	421.87	530.4	421.9
	4.08[13]	517.80	388.68	513.33	382.08	513.2	382.1
	8.80[13]	351.33	−444.72	345.88	−453.13		
	1.27[14]	297.02	−1154.60	294.29	−1148.47		
	2.00[14]	259.93	−2298.42	269.80	−2231.52		
1200 Å	1.41[11]	4.97	−2.32	4.93	−2.32	5.00	−2.32
	4.08[11]	14.37	−4.65	14.29	−4.66	14.51	−4.66
	8.80[11]	30.99	−8.87	30.86	−8.88	31.02	−8.88
	1.27[12]	44.41	−12.38	44.25	−12.39	44.49	−12.39
	2.85[12]	95.69	−27.30	95.44	−27.34	96.50	−27.34
	5.08[12]	151.32	−50.13	150.99	−50.24	151.86	−50.25
	6.88[12]	180.77	−71.51	180.38	−71.72	181.00	−71.73
	9.00[12]	199.80	−100.18	199.31	−100.54	199.75	−100.55
	1.41[13]	210.52	−189.37	209.78	−190.27	209.97	−190.29
	2.03[13]	203.08	−328.67	202.04	−330.46	202.13	−330.44
	3.17[13]	184.39	−617.66	183.02	−620.88	183.2	−620.8
	4.08[13]	172.08	−848.99	170.59	−853.05	170.6	−852.9
	8.80[13]	139.13	−1948.94	139.11	−1947.87		
1600 Å	1.41[11]	0.705	−4.06	0.705	−4.02	0.705	−4.02
	4.08[11]	2.05	−9.67	2.05	−9.63	2.02	−9.63
	8.80[11]	4.42	−19.63	4.42	−19.60	4.42	−19.60
	1.27[12]	6.31	−27.78	6.30	−27.74	6.30	−27.74
	2.85[12]	12.66	−61.08	12.63	−61.03	12.63	−61.03
	5.08[12]	17.20	−108.30	17.12	−108.21	17.12	−108.21
	6.88[12]	18.61	−148.39	18.54	−148.26	18.54	−148.26
	9.00[12]	19.36	−195.96	19.20	−195.75	19.20	−195.75
	1.41[13]	19.78	−313.78	19.54	−313.32	19.54	−313.32
	2.03[13]	19.66	−461.04	19.33	−460.12	19.33	−460.12
	3.17[13]	19.50	−734.22	19.02	−732.35	19.0	−732.3
	4.08[13]	19.72	−948.60	19.13	−946.17	19.2	−946.2
1400 Å	1.41[11]	2.58	−4.51	2.57	−4.51		
	4.08[11]	7.44	−10.95	7.41	−10.95		
	8.80[11]	15.95	−22.31	15.88	−22.31		
	1.27[12]	22.67	−31.53	22.57	−31.53		
	2.85[12]	45.88	−68.74	45.72	−68.75		
	5.08[12]	64.01	−120.89	63.79	−120.94		
	6.88[12]	69.85	−165.65	69.60	−165.73		
	9.00[12]	71.89	−219.99	71.55	−220.13		
	1.41[13]	70.84	−358.79	70.33	−359.10		
	2.03[13]	67.86	−533.64	67.19	−534.06		
	3.17[13]	63.62	−850.74	62.57	−851.21		
	4.08[13]	61.79	−1092.20	60.37	−1092.55		

low intensities, the position and width of this resonance are found to be practically invariant with respect to the inclusion of interblock couplings. At higher intensities, the results of multi-Floquet-block calculations still agree very closely with those obtained from single-Floquet-block, two-channel calculations. Overall, single-Floquet-block calculations are sufficient to ensure convergence for intensities up to $\simeq 10^{14}$ W/cm^2. In contrast, the diabatic results reported by He, Atabek, and Giusti-Suzor [8] in the same intensity range indicate that the first diabatic resonance is strongly affected by the interblock couplings with the resonance positions being more sensitive than their corresponding widths. At intensities approaching 10^{13} W/cm^2, these authors reported convergence with a single-block diabatic integration. However, closer examination of their results reveals that differences between their single-block and multiblock results are more substantial than the corresponding differences in this work, especially in the case of resonance energy shifts. For wavelengths up to 1600 Å, multiblock effects come into play at those crossing points that correspond to multiphoton processes and are located at much higher energies on the repulsive limbs of the potentials belonging to the main Floquet block: the shorter the wavelengths, the higher the left-hand, C^-, crossing points are in energy when compared to the energy of the rightmost crossing point, and hence they do not contribute significantly to the calculation of the resonance energy. Even at high intensities the dynamics is governed mainly by the nonadiabatic couplings between the two adiabatic channels of the main Floquet block. Hence for wavelengths up to 1600 Å, the diagonalization of a single Floquet block (a pure two-channel case) is sufficient to ensure converged results that correspond to single-photon processes. This conclusion is supported by the results presented in Table III, which gives the position and width of the first adiabatic resonance calculated for λ equal to 1000, 1200, and 1600 Å using strictly a single Floquet block compared to those obtained by truncating a multiblock adiabatic set of coupled equations to the two uppermost adiabatic channels.

For longer wavelengths, 1800 and 2000 Å in Table IV, the resonance widths are relatively insensitive to inclusion of multiphoton Floquet blocks, while the resonance energies are strongly affected even at low intensities where the RWA, corresponding to a single-block calculation, is known to be valid. This effect is stronger the longer the wavelength. This low-intensity divergence of the single- from the multiple-Floquet-block adiabatic calculations can be explained with the help of Fig. 2. At these wavelengths, the C^- avoided crossing that corresponds to a three-photon absorption is at an energy low enough to affect the adiabatic nuclear amplitudes $\chi(R)$. At low intensities, the nonadiabatic coupling at this C^- avoided crossing is a δ-function-like singularity that may

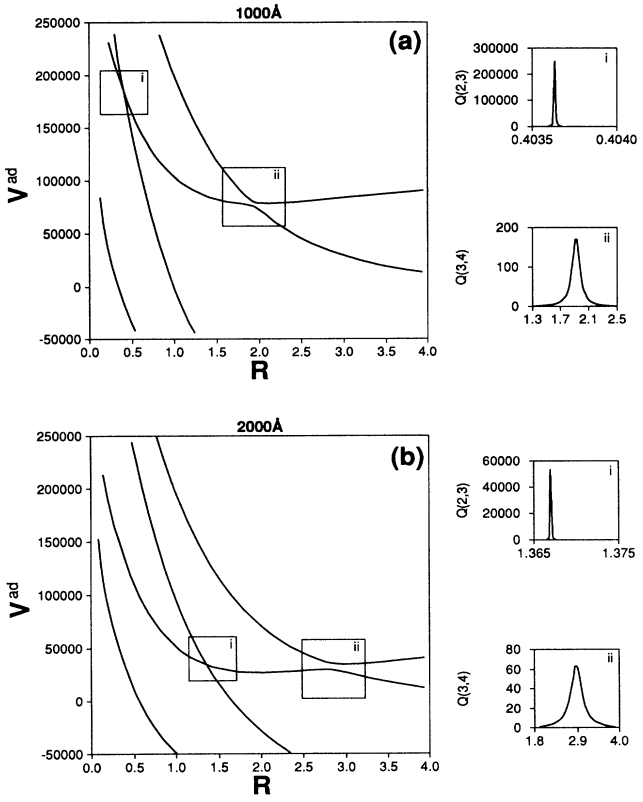

FIG. 2. One-photon and three-photon avoided-crossing regions in the adiabatic potentials (in cm^{-1}) vs R (in a.u.) for (a) $\lambda=1000$ Å and (b) $\lambda=2000$ Å at an intensity of 1.41×10^{13} W/cm^2. The nonadiabatic couplings (in cm$^{-1/2}$) associated with the avoided crossings between the adiabatic channels shown in boxes i and ii are given in the corresponding insets.

TABLE III. Comparison of the shift ΔE and width Γ (in cm^{-1}) of the first $\underline{S}_{\rm red}(E)$ adiabatic resonance of a three-Floquet-block calculation with those of a truncated, three-Floquet-block calculation and those of a one-Floquet-block calculation at an intensity of 4.08×10^{13} W/cm^2.

Diagonalization		Three blocks	Three blocks	One block
Integration		Three blocks	One block	One block
1000 Å	$\Gamma/2$	513.2	513.69	517.80
	ΔE	382.1	382.11	388.68
1200 Å	$\Gamma/2$	170.6	170.81	172.08
	ΔE	−853.0	−852.89	−848.99
1600 Å	$\Gamma/2$	19.2	19.16	19.72
	ΔE	−946.2	−96.16	−98.60

cause numerical instabilities because such a singular coupling cannot be properly taken into account by any integration algorithm. At higher intensities, the calculations of the resonance positions and widths have fully converged because the peaks of the nonadiabatic couplings corresponding to the C^- crossings have broadened and become more tractable for integration. The differences obtained at higher intensities between the two-channel (one-Floquet-block) and four-channel (two-Floquet-block) calculations reflect a true multiblock, i.e., counter-RWA, effect. The observation that the resonance positions are more sensitive to interblock couplings than their widths has also been observed by He, Atabek, and Giusti-Suzor [8] for diabatic resonances.

The results in Tables II and IV are summarized in the plots of $\Delta E/I$ and Γ/I versus log$I$, Fig. 3, ΔE and Γ being the energy shift and the width, respectively, of the first adiabatic resonance obtained using the reduced S matrix. For all wavelengths considered, the variation of resonance positions and widths is linear with intensity up to approximately 10^{13} W/cm^2. The plots for the corresponding first *diabatic* resonance over the same intensity

TABLE IV. Comparison of the shift ΔE and width Γ (in cm^{-1}) of the first adiabatic resonance calculated from the reduced S matrix $\underline{S}_{\text{red}}(E)$ using one and two Floquet blocks for wavelengths 1800 and 2000 Å and for intensities up to 10^{13} W/cm^2.

		Two channels		Four channels	
λ	I (W/cm^2)	$\Gamma/2$	ΔE	$\Gamma/2$	ΔE
1800 Å	1.41[11]	0.125	−3.28	0.126	−1.84
	2.03[11]	0.181	−4.24	0.181	−2.80
	4.08[11]	0.366	−7.43	0.367	−5.99
	8.80[11]	0.801	−14.81	0.803	−13.39
	1.27[12]	1.15	−20.87	1.16	−19.45
	2.03[12]	1.82	−32.90	1.82	−31.50
	2.85[12]	2.42	−45.82	2.42	−44.43
	3.95[12]	3.04	−63.38	3.03	−61.99
	5.08[12]	3.47	−81.28	3.45	−79.89
	6.88[12]	3.90	−111.15	3.88	−109.73
	9.00[12]	4.22	−146.32	4.17	−144.85
	1.14[13]	4.47	−187.02	4.41	−185.43
	1.27[13]	4.58	−209.51	4.51	−207.84
	1.41[13]	4.68	−233.45	4.60	−231.68
	1.70[13]	4.86	−285.79	4.76	−283.76
	2.03[13]	5.03	−344.26	4.90	−341.84
	2.38[13]	5.18	−409.02	5.03	−406.09
	2.76[13]	5.32	−480.24	5.15	−476.65
	3.17[13]	5.46	−558.03	5.26	−553.61
	3.60[13]	5.61	−642.43	5.38	−637.03
	4.08[13]	5.78	−733.43	5.51	−726.89
2000 Å	1.41[11]	0.0161	−2.82	0.0171	14.41
	2.03[11]	0.0235	−3.58	0.0237	13.63
	4.08[11]	0.0477	−6.10	0.0503	11.08
	8.80[11]	0.106	−11.93	0.112	5.15
	1.27[12]	0.155	−16.72	0.163	0.290
	2.03[12]	0.254	−26.21	0.266	−9.35
	2.85[12]	0.356	−36.39	0.372	−19.68
	3.95[12]	0.479	−50.20	0.497	−33.68
	5.08[12]	0.581	−64.21	0.600	−47.89
	6.88[12]	0.704	−87.43	0.723	−71.42
	9.00[12]	0.805	−114.56	0.823	−98.88
	1.14[13]	0.896	−145.75	0.908	−130.40
	1.27[13]	0.940	−162.92	0.949	−147.74
	1.41[13]	0.983	−181.12	0.987	−166.17
	1.70[13]	1.07	−221.03	1.07	−206.34
	2.03[13]	1.16	−265.55	1.15	−251.12
	2.38[13]	1.25	−314.98	1.23	−300.73
	2.76[13]	1.35	−369.58	1.31	−355.40
	3.17[13]	1.45	−429.60	1.41	−415.39
	3.60[13]	1.55	−495.32	1.49	−480.89
	4.08[13]	1.66	−566.95	1.59	−552.15

range can be found in Ref. [8]. The relative ordering of the curves with respect to wavelengths is the same as in the diabatic case but the positions and widths of the resonance differ; the diabatic and adiabatic resonances are not unitary equivalents.

B. Adiabatic Feshbach and shape resonances

The results presented in the previous section were obtained by analyzing the reduced S matrix $\underline{S}_{\rm red}(E)$ and have served to delineate multiblock effects in the adiabatic representation. For field intensities $\leq 10^{13}$ W/cm^2, intensities at which these effects are negligible, single-Floquet-block integrations have been performed to identify higher adiabatic resonances in $\underline{S}_{\rm red}(E)$ as well as resonances in the unreduced S matrix $\underline{S}(E)$ and the uncoupled (open-channel) S matrix $\underline{S}_0$.

As discussed previously, in the adiabatic representation $\underline{S}_0$ can support resonances of the type *shape*. It is to be expected that these resonances will interfere with the adiabatic Feshbach resonances at high intensities. Because of the possibility of overlap between the shape and Feshbach resonances, care must be exercised when classifying

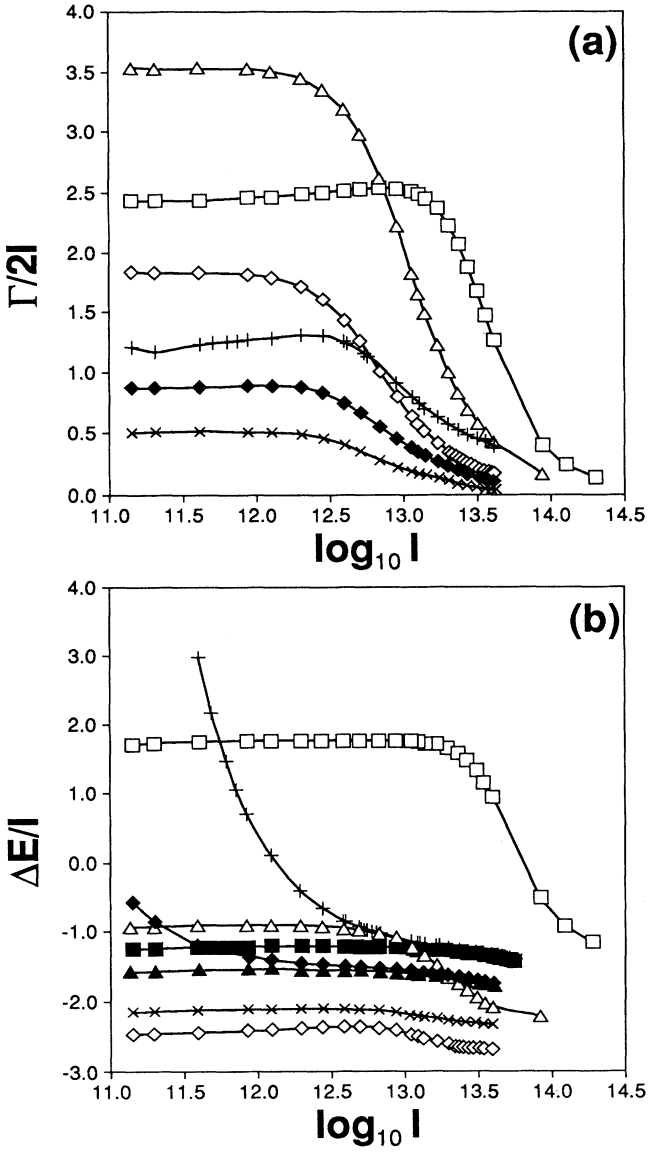

FIG. 3. Variation of (a) $\Gamma/2I$ and (b) $\Delta E/I$ (in 10^{-11} cm/W) versus log$I$ for λ equal to 1000 Å (□), 1200 Å (△), 1400 Å (◇), 1600 Å (×), 1800 Å (◆), and 2000 Å (+) calculated using two Floquet blocks. In (a), the 1800-Å results have been multiplied by 10 and the 2000-Å results have been multiplied by 100. In (b) the two-channel results for 1800 Å (▲) and 2000 Å (■) have been included.

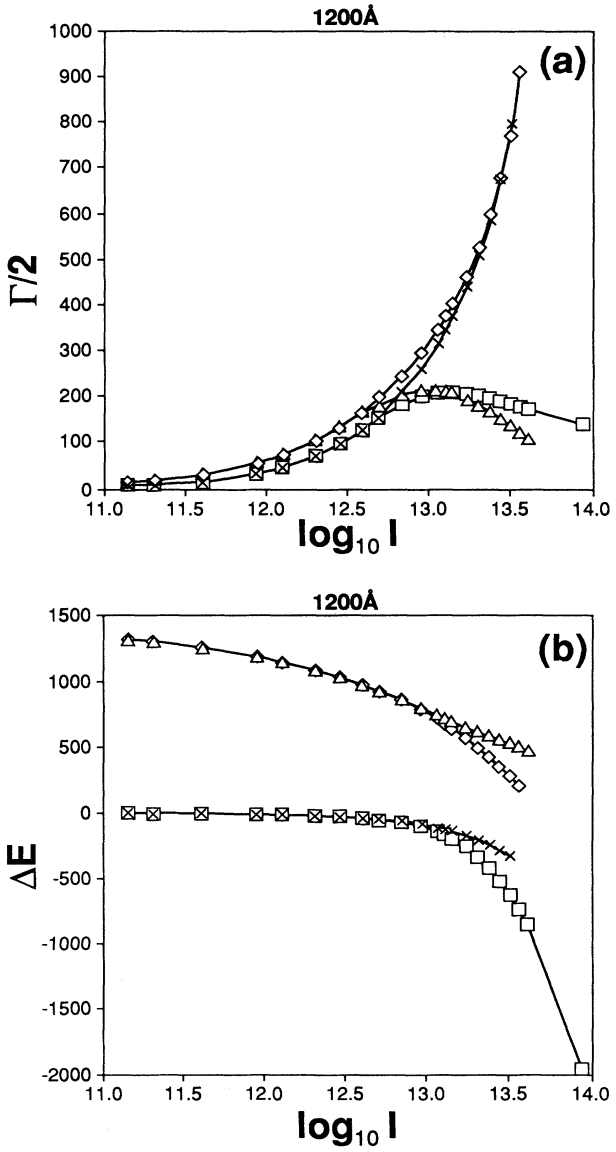

FIG. 4. Plots of (a) $\Gamma/2$ and (b) ΔE (in cm^{-1}) vs log$I$ for the first (□) $\underline{S}_{\rm red}(E)$ resonance, the second (△) $\underline{S}_{\rm red}(E)$ resonance, the first $\underline{S}_0$ (◇) resonance, and the first (×) $\underline{S}(E)$ resonance calculated using a single Floquet block for λ equal to 1200 Å.

TABLE V. Shifts ΔE and widths Γ (in cm^{-1}) of resonances calculated using one Floquet block and the unreduced S matrix $\underline{S}(E)$ for the wavelengths 1000, 1200, 1400, and 1600 Å and for intensities up to 10^{13} W/cm^2.

$\underline{S}(E)$	1000 Å		1200 Å		1400 Å		1600 Å	
I (W/cm^2)	$\Gamma/2$	ΔE	$\Gamma/2$	ΔE	$\Gamma/2$	ΔE	$\Gamma/2$	ΔE
1.41[11]	3.42	1.40	4.95	−2.32	2.57	−4.51	0.704	−4.06
2.03[11]	4.92	2.50	7.12	−2.85	3.70	−6.01	1.02	−5.36
4.08[11]	9.88	6.11	14.21	−4.65	7.39	−10.95	2.05	−9.67
8.80[11]	21.34	14.48	30.34	−8.87	15.87	−22.31	4.48	−19.63
1.27[12]	30.71	21.33	43.25	−12.38	22.71	−31.52	6.50	−27.77
2.03[12]	49.22	34.89	68.06	−19.45	36.02	−49.53	10.60	−43.84
2.85[12]	68.99	49.38	93.56	−27.18	49.94	−68.47	15.10	−60.95
3.95[12]	95.70	68.93	126.52	−37.90	68.30	−93.56	21.40	−83.93
5.08[12]	122.73	88.65	158.25	−48.97	86.42	−118.36	27.99	−106.99
6.88[12]	167.56	121.00	207.58	−67.65	115.47	−158.06	39.30	−144.59
9.00[12]	220.26	158.17	260.92	−89.77	148.17	−202.35	53.04	−187.47
1.14[13]	282.02	199.97	317.80	−115.29	184.51	−250.76	69.46	−235.36
1.27[13]	316.94	222.50	347.54	−129.30	204.11	−276.36	78.75	−126.10
1.41[13]	355.16	246.05	378.19	−144.09	224.71	−302.81	88.81	−287.96
1.70[13]	445.49	295.83	442.52	−175.92	269.15	−358.02	111.35	−344.91
2.03[13]			511.89	−210.43	318.58	−415.92	137.39	−405.84
2.38[13]			588.54	−247.22	374.27	−476.07	167.32	−470.33
2.76[13]			677.39	−285.79	438.76	−538.01	201.61	−537.99
3.17[13]			800.03	−325.67	519.43	−601.29	240.98	−608.40
3.60[13]							286.51	−681.14
4.08[13]							340.34	−755.82

resonances obtained from adiabatic S-matrix analysis. For wavelengths up to 1600 Å, the results of two-channel calculations of the first resonances in the unreduced $\underline{S}(E)$ and the uncoupled $\underline{S}_0$ are given in Tables V and VI, respectively, and the resonances found at higher energies through the phase analysis of $\underline{S}_{red}(E)$ are given in Table VII for λ equal to 1000 Å and in Table VIII for λ equal to 1200, 1400, and 1600 Å. At low intensities, the first resonance in $\underline{S}(E)$ (Table V) coincides with the first resonance in $\underline{S}_{red}(E)$ (Table II), while the first shape resonance in $\underline{S}_0$ is found at a much higher energy (Table VI). This indicates that no overlap occurs at low intensities.

TABLE VI. Shifts ΔE and widths Γ (in cm^{-1}) of resonances calculated using one Floquet block and the uncoupled S matrix $\underline{S}_0$ for the wavelengths 1000, 1200, 1400, and 1600 Å and for intensities up to 10^{13} W/cm^2.

$\underline{S}_0$	1000 Å		1200 Å		1400 Å		1600 Å	
I (W/cm^2)	$\Gamma/2$	ΔE	$\Gamma/2$	ΔE	$\Gamma/2$	ΔE	$\Gamma/2$	ΔE
1.41[11]	17.29	3755.30	10.62	1321.85	5.30	415.57	2.00	110.31
2.03[11]	24.30	3723.91	14.83	1303.04	7.34	405.60	2.74	105.69
4.08[11]	45.74	3647.98	27.59	1257.62	13.46	381.31	4.90	94.15
8.80[11]	88.88	3534.06	52.94	1189.06	25.48	343.65	9.07	75.09
1.27[12]	119.66	3467.37	70.97	1148.32	34.06	320.40	12.03	62.46
2.03[12]	172.72	3367.17	102.19	1085.71	49.14	282.95	17.31	40.67
2.85[12]	221.61	3285.28	131.31	1032.82	63.57	249.44	22.52	19.70
3.95[12]	279.21	3197.28	166.21	973.81	81.42	209.85	29.22	−6.70
5.08[12]	330.66	3124.41	197.98	922.99	98.27	173.83	35.85	−32.10
6.88[12]	405.52	3025.83	245.34	851.09	124.44	119.89	46.73	−73.23
9.00[12]	482.06	2932.59	295.14	779.52	153.28	62.92	59.55	−116.98
1.14[13]	560.71	2843.70	347.69	707.98	185.06	2.96	74.59	−166.32
1.27[13]	601.04	2800.67	375.14	672.17	202.15	−28.09	83.04	−192.68
1.41[13]	642.18	2758.50	403.48	636.32	220.10	−59.82	92.16	−220.12
1.70[13]	727.43	2676.51	463.18	564.57	258.77	−125.18	112.57	−278.18
2.03[13]	817.79	2597.47	527.77	492.80	301.60	−192.81	136.14	−340.22
2.38[13]	915.14	2521.25	598.78	421.18	349.30	−262.37	163.23	−405.90
2.76[13]	1022.54	2447.81	678.78	349.93	402.96	−333.49	194.27	−474.87
3.17[13]	1146.22	2377.23	773.50	279.26	464.42	−405.78	229.78	−546.72
3.60[13]	1309.72	2309.62	914.23	209.47	537.71	−478.84	270.52	−621.07
4.08[13]					642.99	−552.28	317.65	−697.52

TABLE VII. Shifts ΔE and widths Γ (in cm^{-1}) of three upper adiabatic resonances calculated using one Floquet block and the reduced S matrix $\underline{S}_{red}(E)$ for $\lambda = 1000$ Å and for intensities up to 10^{13} W/cm^2.

	Second resonance		Third resonance		Fourth resonance	
$I(W/cm^2)$	$\Gamma/2$	ΔE	$\Gamma/2$	ΔE	$\Gamma/2$	ΔE
1.41[11]			1.65	2234.91	17.38	3755.30
2.03[11]			2.37	2234.92	24.48	3723.91
4.08[11]			4.75	2234.96	46.36	3647.98
8.80[11]	93.90	1365.70	10.20	2235.01	91.07	3534.06
1.27[12]	60.16	1389.91	14.58	2235.00	123.32	3467.38
2.03[12]	33.70	1418.08	22.95	2234.89	178.75	3367.28
2.85[12]	22.35	1438.41	31.37	2234.61	227.53	3285.71
3.95[12]	15.13	1459.49	41.69	2233.98	276.74	3198.96
5.08[12]	11.37	1476.60	50.76	2233.07	306.74	3129.09
6.88[12]	8.25	1498.75	62.82	2231.00	320.23	3042.29
9.00[12]	6.78	1517.36	73.25	2227.89	303.59	2978.94
1.14[13]	6.53	1531.61	82.19	2223.76	273.97	2948.13
1.27[13]	6.82	1537.03	86.26	2221.40	259.42	2945.73
1.41[13]	7.41	1541.38	90.13	2218.94	246.46	2951.26
1.70[13]	9.54	1547.40	97.25	2214.13	226.41	2981.94
2.03[13]	12.87	1550.98	103.14	2210.50	212.75	3032.04
2.38[13]	16.81	1553.75	106.70	2209.88	202.98	3093.93
2.76[13]	19.95	1557.87	106.51	2214.76	194.19	3160.87
3.17[13]	20.37	1566.61	101.43	2227.97	183.43	3226.64
3.60[13]	17.00	1584.38	91.34	2251.84	168.57	3285.51
4.08[13]	10.83	1615.50	77.42	2287.68	149.45	3332.82

Hence at these intensities, the resonances presented and discussed in the previous section, Tables II, III, and IV, can be identified as true adiabatic Feshbach resonances. At higher intensities, the position and width of the first $\underline{S}(E)$ resonance deviates strongly from those of the first $\underline{S}_{red}(E)$ resonance, indicating significant resonance overlap. Perusal of the first $\underline{S}_0$ resonance data, Table VI, reveals a common trend for the four wavelengths under consideration: at high intensities, the position of the shape resonance is lowered and its width increases

TABLE VIII. Shifts ΔE and widths Γ (in cm^{-1}) of the adiabatic upper resonances calculated using one Floquet block and the reduced S matrix $\underline{S}_{red}(E)$ for the wavelengths 1200, 1400, and 1600 Å and for intensities up to 10^{13} W/cm^2.

	1200 Å		1400 Å		1600 Å	
I (W/cm^2)	$\Gamma/2$	ΔE	$\Gamma/2$	ΔE	$\Gamma/2$	ΔE
1.41[11]	10.68	1321.84	5.32	415.57	2.00	110.31
2.03[11]	14.95	1303.04	7.38	405.60	2.75	105.69
4.08[11]	27.98	1257.62	13.57	381.31	4.91	94.15
8.80[11]	54.22	1189.06	25.68	343.66	8.99	75.09
1.27[12]	72.99	1148.33	34.05	320.42	11.69	62.47
2.03[12]	105.07	1085.77	47.48	283.08	15.74	40.76
2.85[12]	133.41	1033.04	57.82	249.91	18.41	20.04
3.95[12]	163.30	974.57	66.40	211.37	20.12	−5.62
5.08[12]	184.86	924.89	70.64	177.43	20.60	−29.59
6.88[12]	205.29	856.89	72.13	129.59	20.40	−65.89
9.00[12]	213.11	794.00	70.94	83.48	19.92	−104.44
1.14[13]	211.12	738.27	68.37	39.24	19.44	−145.34
1.27[13]	207.70	713.50	67.05	17.65	19.21	−166.71
1.41[13]	203.25	690.80	65.32	−3.72	18.99	−188.71
1.70[13]	192.47	651.11	61.97	−46.14	18.51	−234.56
2.03[13]	180.26	617.58	58.37	−88.61	17.99	−282.82
2.38[13]	167.13	588.27	54.50	−131.59	17.39	−333.36
2.76[13]	153.26	561.31	50.41	−175.39	16.69	−386.03
3.17[13]	138.83	535.15	46.15	−220.24	15.88	−440.68
3.60[13]	124.10	508.55	41.77	−266.33	14.94	−497.17
4.08[13]	109.42	480.59	37.35	−313.79	13.89	−555.39

significantly. These effects may become sufficiently strong to create an effective overlap between the first shape resonance and the lower-lying first Feshbach resonance. Furthermore, a higher-energy resonance in $\underline{S}_{red}(E)$, Tables VII and VIII, coincides with the first $\underline{S}_0$ resonance at low intensities, indicating that this resonance is initially a pure shape resonance. At higher intensities it deviates from the pure $\underline{S}_0$ shape resonance, which again reflects overlap between the shape and Feshbach resonances. The 1200-, 1400-, and 1600-Å results in Tables II and VIII indicate that the overlap involves only the first Feshbach resonance. However, the results for λ equal to 1000 Å in Table VII suggest that two additional Feshbach resonances, found at higher energies, strongly overlap with the first shape resonance associated with $\underline{S}_0$, while the first Feshbach resonance is only remotely affected by this shape resonance (Table II). Note the presence of a minimum in the variation of the width of the 1000-Å second resonance with respect to intensity (Table VII). This stabilization of the second adiabatic Feshbach resonance denotes the formation of a long-lived, quasi-bound adiabatic state as a consequence of resonance overlap. For other wavelengths (Table VIII), as

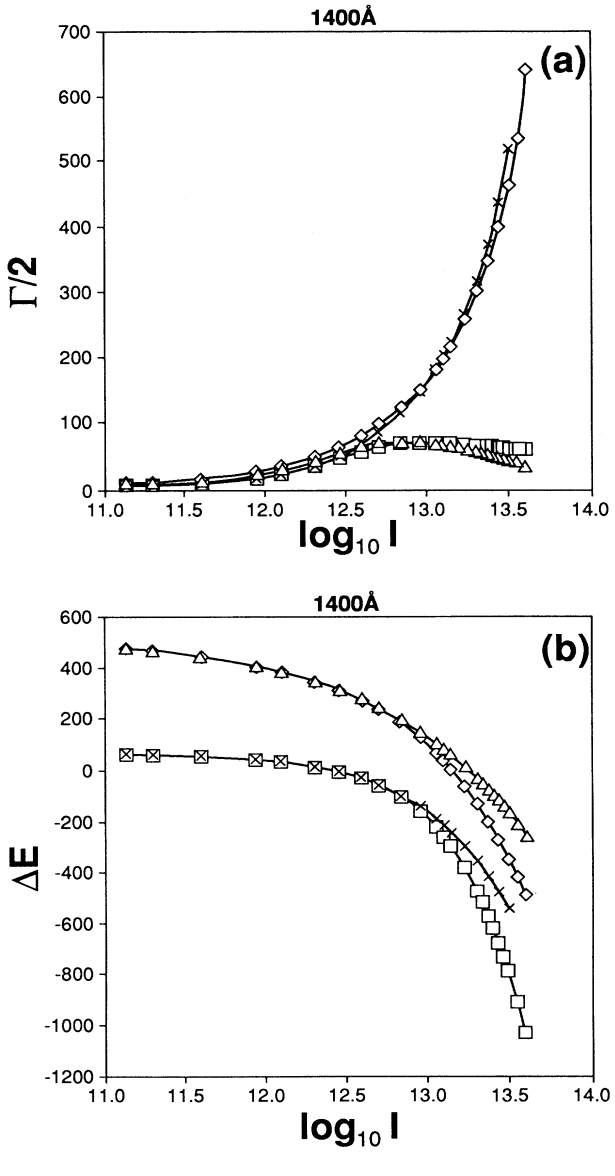

FIG. 5. Plots of (a) $\Gamma/2$ and (b) ΔE (in cm^{-1}) vs log$I$ for the first (□) $\underline{S}_{red}(E)$ resonance, the second (△) $\underline{S}_{red}(E)$ resonance, the first $\underline{S}_0$ (◇) resonance, and the first (×) $\underline{S}(E)$ resonance calculated using a single Floquet block for λ equal to 1400 Å.

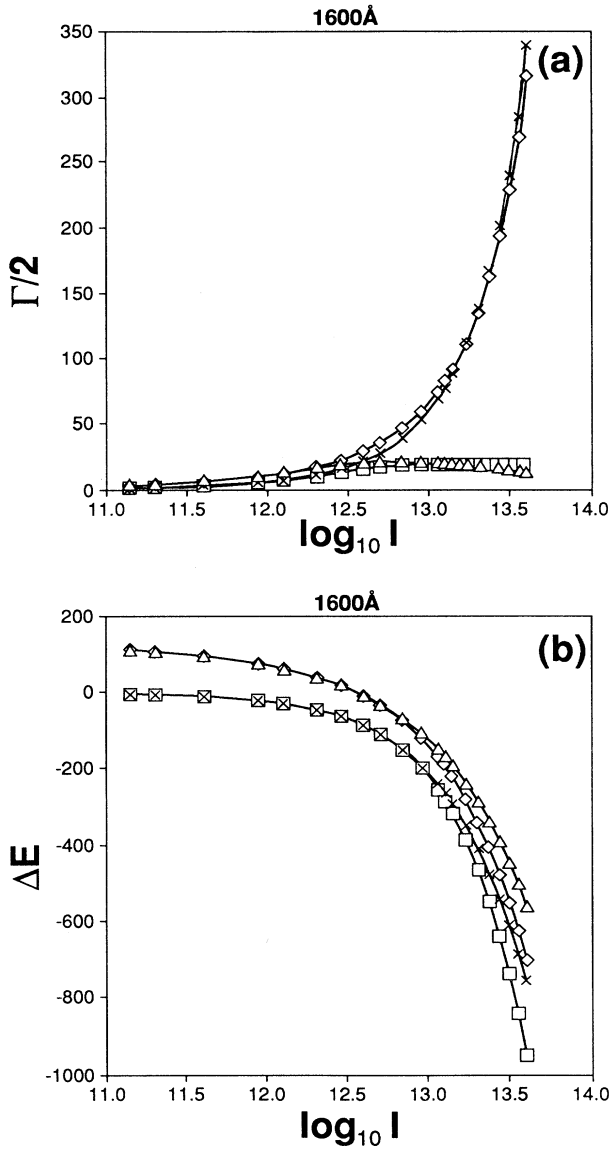

FIG. 6. Plots of (a) $\Gamma/2$ and (b) ΔE (in cm^{-1}) vs log$I$ for the first (□) $\underline{S}_{red}(E)$ resonance, the second (△) $\underline{S}_{red}(E)$ resonance, the first $\underline{S}_0$ (◇) resonance, and the first (×) $\underline{S}(E)$ resonance calculated using a single Floquet block for λ equal to 1600 Å.

well as for the third and fourth 1000-Å adiabatic resonances in Table VII, the decrease in magnitude of the width with respect to increasing intensity indicates that similar stabilizations also occur at yet higher intensities. The behavior of the shape and Feshbach resonances discussed above at high field intensities is summarized in Figs. 4, 5, and 6 for λ equal to 1200, 1400, and 1600 Å, respectively, and in Fig. 7 for λ equal to 1000 Å. It is interesting to note that for λ equal to 1000 Å, the uncoupled open-channel wave function supports shape resonances only because $\tilde{W}^{\text{ad}}_{\pm}(R)$ of (45) contains a potential well created by including the diagonal correction term

$$|Q_{12}(R)|^2=\frac{\hbar^2}{2\mu}\left[\frac{d}{dR}\vartheta(R)\right]^2 \tag{62}$$

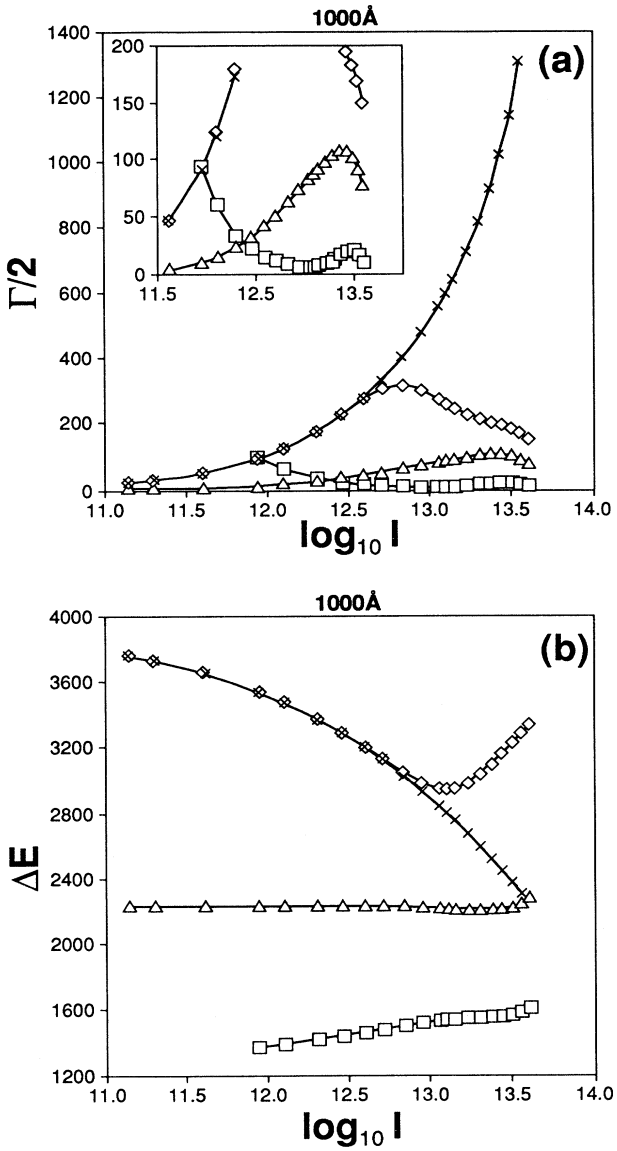

FIG. 7. Plots of (a) $\Gamma/2$ and (b) ΔE (in cm^{-1}) vs $\log I$ for the first $\underline{S}_0$(×) resonance as well as the second (□), third (△), and fourth (◇) $\underline{S}_{\text{red}}(E)$ resonances calculated using a single Floquet block for λ equal to 1000 Å.

[see (48)]. This effect is depicted in Fig. 8. The field-induced tunneling barrier described by (62) varies inversely with field intensity I, and hence the first shape resonance is expected to be lowered and to broaden as I increases. This is observed in all cases.

V. CONCLUSIONS

The distinction between diabatic and adiabatic resonances has been demonstrated formally, i.e., the nonequivalence of $\hat{L}_{Q'Q'}[\hat{\mathcal{H}}]$ and $\hat{L}_{QQ}[\hat{\mathcal{H}}]$ shown in Sec. II. B.

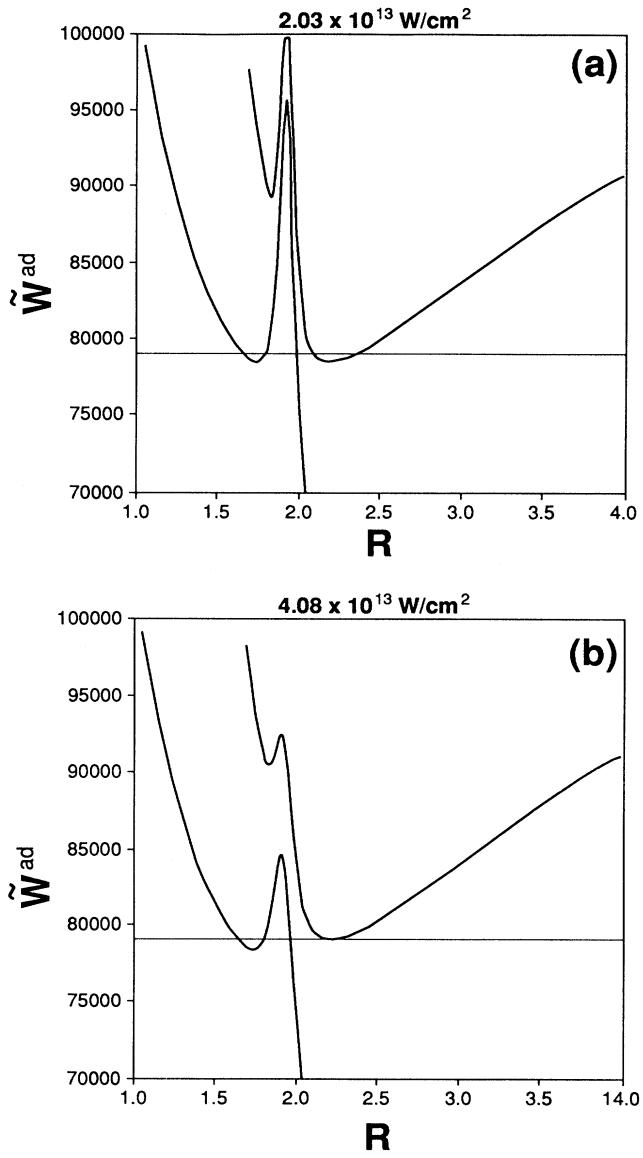

FIG. 8. Plots of $\tilde{W}^{\text{ad}}_{\pm}(R)$ (in cm^{-1}) vs R (in a.u.) calculated using a single Floquet block with λ equal to 1000 Å for intensities of (a) 2.03×10^{13} W/cm^2 and (b) 4.08×10^{13} W/cm^2 showing the variation of the height and shape of the nonadiabatic tunneling barrier at the avoided crossing with respect to intensity. The horizontal line represents the position of the first $\underline{S}_{\text{red}}$ resonance.

Physically, this distinction is reflected by the role played by the resonance width in the diabatic and adiabatic representations in the low- and high-intensity regimes, respectively. At low intensities, in the so-called Markovian regime [26], the diabatic resonance width is a direct measure of the photodissociation rate. As the intensity is increased, the resonance states should be properly interpreted as intermediates through which the system transits towards a final dissociative state [9]: no single diabatic resonance width is a direct measure of the photodissociation rate. Hence the diabatic representation is appropriate for the low-intensity regime. On the other hand, the adiabatic resonances exhibit the opposite behavior with respect to intensity and represent physical dressed states only at high intensities. At low intensities, the strong nonadiabatic couplings prevent the direct association of an adiabatic resonance width with a photodissociation rate via the usual perturbative arguments.

In spite of these formal and physical distinctions, numerical coincidences of diabatic and adiabatic resonances must occur when radiative coupling potentials in the diabatic representation vanish asymptotically. Such is not the case in the present problem, where the diabatic radiative interaction described in the so-called electric-field gauge [27] involves an asymptotically divergent transition dipole moment. Hence this explains the numerical differences between the diabatic and adiabatic resonances observed in Sec. IV. The same problem recast in the radiation field gauge will involve radiative interactions that vanish asymptotically as shown in Ref. [17]. Consequently, coincidences of diabatic and adiabatic resonances are expected to occur in this gauge. This behavior is the object of current investigations.

ACKNOWLEDGMENTS

We wish to thank Professor O. Atabek (Orsay, France) and Professor A. D. Bandrauk (Sherbrooke, Canada) for stimulating discussions. The financial support of the Natural Sciences and Engineering Research Council of Canada (NSERC) is gratefully acknowledged. This work is also partially supported by the Network of Centres of Excellence Programme in association with NSERC, through the Centre of Excellence for Molecular and Interfacial Dynamics (CEMAID).

[1] N. M. Kroll and K. M. Watson, Phys. Rev. A **13**, 1018 (1976).
[2] A. M. F. Lau and C. K. Rhodes, Phys. Rev. A **16**, 2392 (1977); A. M. F. Lau, *ibid.* **13**, 139 (1976).
[3] T. F. George, J. Phys. Chem. **86**, 10 (1982); T. F. George, I. H. Zimmerman, J.-M. Yuan, J. R. Laing, and P. L. DeVries, Acc. Chem. Res. **10**, 449 (1977).
[4] T. T. Nguyen-Dang and A. D. Bandrauk, J. Chem. Phys. **80**, 4926 (1984); **79**, 3256 (1983).
[5] A. D. Bandrauk and O. Atabek, in *Lasers, Molecules and Methods,* edited by J. O. Hirschfelder, R. E. Wyatt, and R. D. Coalson (Wiley, New York, 1989), Vol. LXXIII, p. 823.
[6] A. D. Bandrauk and M. L. Sink, J. Chem. Phys. **74**, 1110 (1981).
[7] M. Shapiro and H. Bony, J. Chem. Phys. **83**, 1588 (1985).
[8] X. He, P. Atabek, and A. Giusti-Suzor, Phys. Rev. A **38**, 5586 (1988).
[9] A. D. Bandrauk and G. Turcotte, J. Phys. Chem. **89**, 3039 (1985).
[10] A. D. Bandrauk and G. Turcotte, J. Chem. Phys. **77**, 3867 (1982).
[11] A. D. Bandrauk and G. Turcotte, J. Phys. Chem. **87**, 5098 (1983).
[12] S.-I. Chu, in *Lasers, Molecules and Methods* (Ref. 5), Vol. LXXIII, p. 739.
[13] S.-I. Chu, J. Chem. Phys. **75**, 2215 (1981).
[14] X. He, Ph.D. thesis, Université de Paris-Sud, Orsay, France, 1989.
[15] T. T. Nguyen-Dang, S. Durocher, and O. Atabek, Chem. Phys. **129**, 451 (1989).
[16] S. Durocher, M. Sc. thesis, Université de Sherbrooke, Sherbrooke, Quebec, Canada, 1989.
[17] X. He, O. Atabek, and A. Giusti-Suzor, Phys. Rev. A **42**, 1585 (1990).
[18] A. Giusti-Suzor, X. He, O. Atabek, and F. H. Mies, Phys. Rev. Lett. **64**, 515 (1990).
[19] A. Zavriyev, P. H. Bucksbaum, H. G. Muller, and D. W. Schumacher, Phys. Rev. A **42**, 5500 (1990).
[20] P. H. Bucksbaum, A. Zavriyev, H. G. Muller, and D. W. Schumacher, Phys. Rev. Lett. **64**, 1883 (1990).
[21] A. D. Bandrauk (private communication).
[22] C. L. Shoemaker and R. E. Wyatt, Adv. Quantum Chem. **14**, 169 (1981).
[23] H. Feshbach, Ann. Phys. (N.Y.) **19**, 287 (1962); **5**, 357 (1958).
[24] The superscript 0 in (31) is used to differentiate $G_{PP}^{+}[\hat{\mathcal{H}}]=\lim_{\epsilon\to 0+}\hat{P}(E+i\varepsilon-\hat{\mathcal{H}})^{-1}\hat{P}$ from $G_{PP}^{0+}[\hat{\mathcal{H}}]$. The positive sign is selected to ensure that the second term of (28) contains outgoing waves.
[25] F. V. Bunkin and I. I. Tugov, Phys. Rev. A **8**, 601 (1973).
[26] R. D. Gilbert and R. N. Porter, J. Chem. Phys. **89**, 3057 (1988).
[27] A. D. Bandrauk, O. F. Kalman, and T. T. Nguyen-Dang, J. Chem. Phys. **84**, 6761 (1986).